Chemical-guided SHAPE sequencing (cgSHAPE-seq) informs the binding site of RNA-degrading chimeras targeting SARS-CoV-2 5' untranslated region

Zhichao Tang[1,3], Shalakha Hegde[1,3], Siyuan Hao[2], Manikandan Selvaraju[1], Jianming Qiu[2], Jingxin Wang*[1]

[1]Department of Medicinal Chemistry, University of Kansas, Lawrence, KS, USA.

[2]Department of Microbiology, Molecular Genetics and Immunology, University of Kansas Medical Center, Kansas City, KS, USA.

[3]These authors contributed equally.

*Email: wang.jingxin@ku.edu

One of the hallmarks of RNA viruses is highly structured untranslated regions (UTRs) in their genomes. These conserved RNA structures are often essential for viral replication, transcription, or translation. In this report, we discovered and optimized a new coumarin derivative **C30** that binds to a four-way RNA helix called SL5 in the 5' UTR of the SARS-CoV-2 RNA genome. To locate the binding site, we developed a novel sequencing-based method namely cgSHAPE-seq, in which the acylating chemical probe was directed to crosslink with the 2'-OH groups of ribose at the ligand binding site. This crosslinked RNA could then create read-through mutations during reverse transcription (i.e., primer extension) at single-nucleotide resolution to uncover the acylation locations. cgSHAPE-seq unambiguously determined that a bulged G in SL5 was the primary binding site of **C30** in the SARS-CoV-2 5' UTR, which was validated through mutagenesis and in vitro binding experiments. **C30** was further used as a warhead in RNA-degrading chimeras (RIBOTACs) to reduce viral RNA expression levels. We demonstrated that replacing the acylating moiety in the cgSHAPE probe with ribonuclease L recruiter (RLR) moieties yielded RNA degraders active in the in vitro RNase L degradation assay and SARS-CoV-2 5' UTR expressing cells. We further explored another RLR conjugation site on the E ring of **C30** and discovered potent activity in vitro and in cells. The optimized RIBOTAC **C64** inhibited live virus replication in lung epithelial carcinoma cells.

RNA viruses usually have highly structured 5' and 3' UTRs in their RNA genome, which can potentially serve as therapeutic targets[1]. In this report, we used SARS-CoV-2 as a specific test-case example and explore to use RNA-degrading chimeras to inhibit virus replication. SARS-CoV-2 is an enveloped ssRNA(+) virus. The whole genome of SARS-CoV-2 (~30,000 nucleotides) is encoded in a single RNA molecule[2]. The viral RNA in transmitted virions is 5' capped and 3' polyadenylated, so that it is recognized and treated as an mRNA[3]. In this step, the 5' UTR is used to hijack the host ribosome to translate viral proteins[4]. Furthermore, the 5'

38 UTR plays an essential role in RNA transcription for each coronavirus structural protein, which
39 is accomplished through a "discontinuous" transcription mechanism. Specifically, the replication
40 transcription complex binds to the 5' UTR leader transcriptional regulatory sequences (TRS-L),
41 and then "hops" onto the body TRS (TRS-B) sequence located at the 5'-end of each structural
42 gene[5,6]. That said, all SARS-CoV-2 transcripts share the same 5' UTR leader sequence. In
43 addition, the SARS-CoV-2 5' UTR was reported essential for viral RNA packaging[7].

44 Given the importance of the UTRs in SARS-CoV-2, we and others elucidated the RNA
45 structures in SARS-CoV-2 UTRs[8–12]. The 5' UTR RNA structures in cell-free buffers, in virus-
46 infected cells, and in our reporter cell model are highly consistent [8–13], suggesting superior
47 stability and suitability serving as drug targets. The 5' UTR of SARS-CoV-2 contains five stem-
48 loops, namely SL1–5. The start codon resides in SL5, a unique four-way helix[8–12] (Fig. 1a). SL5
49 exists in all betacoronavirus species, including MERS and SARS-CoV, and the shapes of this
50 RNA structure are similar[9]. We aligned the SARS-CoV-2 RefSeq and different lineages and
51 demonstrated that the SL5 is highly conserved among all strains[1]. Although a predominant
52 mutation was found in SL5B loop region from recent lineages (C241T), this mutation is unlikely
53 to change the overall structure of SL5[1]. In SARS-CoV-2, several structures in the 5' UTR,
54 including SL4, SL5A, and SL6, were found binding to amilorides[14] (Fig. 1a). Amilorides
55 demonstrated antiviral activity in SARS-CoV-2 infected cells.

56 Here, we report a pipeline in antiviral discovery and optimization of RNA-degrading chimeras
57 targeting SL5, highlighting a novel sequencing-based method namely chemical-guided (cg)
58 selective 2′-hydroxyl acylation analyzed by primer extension (SHAPE) sequencing (seq), or
59 cgSHAPE-seq, to rapidly locate the RNA ligand binding site (Fig. 1a). First, we screened a small
60 coumarin derivative library in SL5 RNA binding assay and optimized the hit through structure-
61 activity-relationship studies. To elucidate the RNA ligand binding site, we synthesized and
62 applied a new type of chemical probe that can selectively acylate the 2'-OH on the ribose at the
63 location of binding (Fig. 1b)[26,27]. The 2'-OH acylation locations were "recorded" onto RNA
64 molecules by reverse transcriptase as single-point mutations at the modification sites during
65 primer extension. The mutation sites were then captured and deconvoluted by next-generation
66 sequencing[28,29]. Mutational profiling analysis in cgSHAPE-seq unambiguously identified a
67 bulged G in SL5 as the primary binding site in the SARS-CoV-2 5' UTR. In the literature, other
68 sequencing-based methods were reported using affinity probes bearing nitrogen mustard or
69 diazirine moiety (e.g., ChemCLIP-seq[15–19] and PEARL-seq[20]). However, a major limitation of
70 these methods is a strong labeling bias toward guanosines[21]. Similar to the SHAPE, cgSHAPE-
71 seq reacts with 2'-OH of A, U, G, or C at similar rates. This can potentially increase the scope
72 and accuracy of proximity-induced chemical reactions on RNAs for mapping purposes.

73 We further developed RNA-degrading chimeras by replacing the 2'-OH acylating moiety with
74 RNase L recruiter (RLR) moieties on the cgSHAPE probe, as well as by conjugating the RLR
75 moieties on other putative solvent accessible site on the RNA ligand. RNA-degrading chimera
76 utilizing endogenous ribonuclease (RNase) L was first reported by the Silverman group in
77 1993[22]. Recently, the modality of RNA-degrading chimera was further developed by the Disney
78 group and was demonstrated to be active using small-molecule RNA ligands[23–30] (Fig. 1c). The
79 Disney group also coined the name ribonuclease targeting chimera or RIBOTAC for this type of

80   RNA degraders. RIBOTACs were shown efficacious to degrade microRNA in cells[24,25] and
81   mouse models[26]. Importantly, a small-molecule RIBOTAC was recently used to degrade the
82   SARS-CoV-2 RNA genome by targeting an RNA structure named attenuator hairpin near the
83   programmed frameshift (PFS) regulatory element[23]. The viral RNA transcript level was shown to
84   be reduced in a model cell system by ~50% at 8 µM RIBOTAC[23]. Antisense-based RNA-
85   degrading chimeras targeting spike-protein or envelope-protein encoding RNAs were also
86   demonstrated efficacy in SARS-CoV-2 infected cells[28]. Our optimized RIBOTAC robustly
87   degraded SARS-CoV-2 RNA in cellular models at 1 µM and inhibited virus replication at 20 µM
88   in lung epithelial cells. No significant toxicity was observed. Interestingly, we discovered the
89   natural RNase L binding moiety is similar or less active than the synthetic RLR in the RIBOTAC
90   modality.
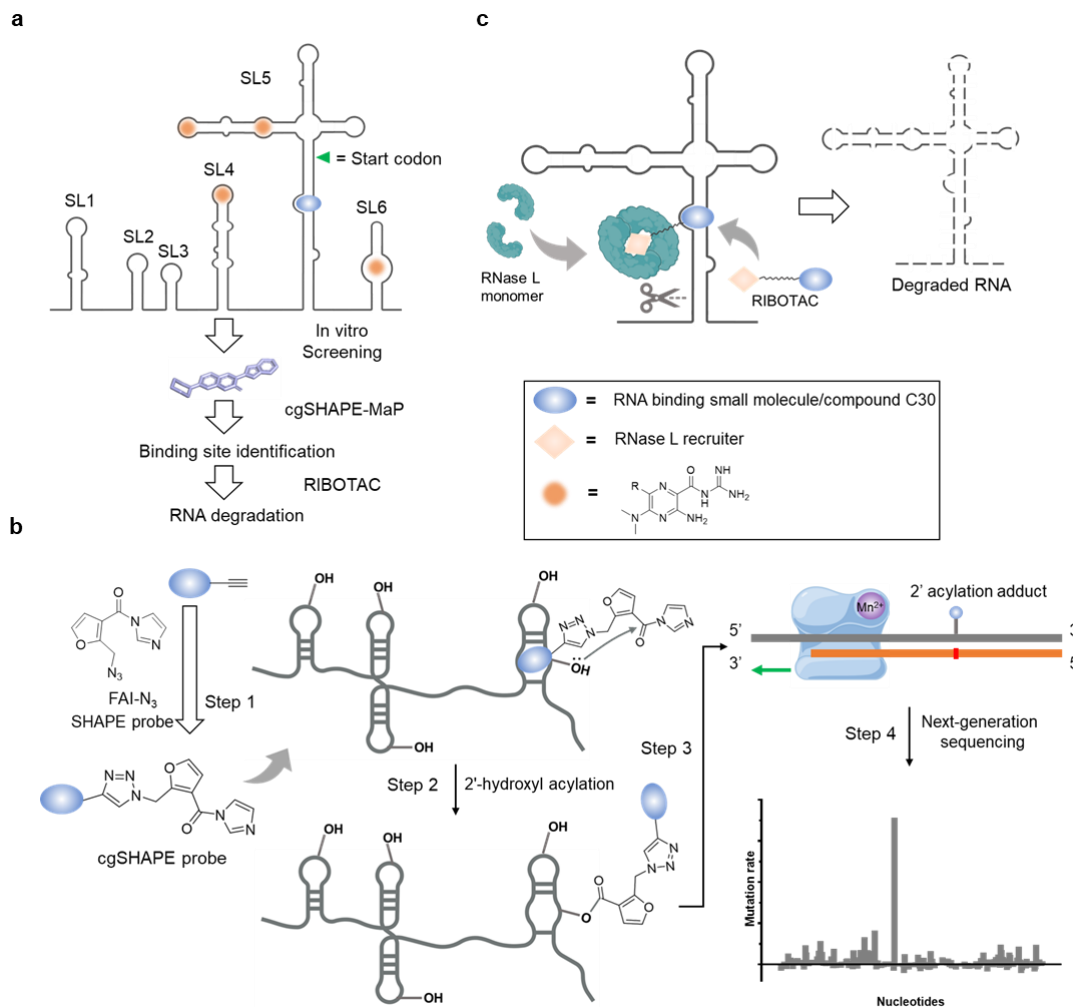
91

92   **Fig. 1 | Development of cgSHAPE-seq and anti-viral RIBOTAC. a**, RNA secondary structures in SARS-CoV-2 5'
93   UTR and the pipeline in identification of the ligand binding site and the development of RNA-degrading chimeras. **b**,
94   Principle of cgSHAPE-seq for identifying small molecule binding sites in four steps. Step 1: Synthesis of FAI conjugated
95   chemical probe. Step 2: Chemical-guided acylation at the 2'-OH of ribose at the binding site. Step 3: Reverse
96   transcription in the presence of Mn^{2+} creates single-point mutations at the acylation site. Step 4: Mutational profiling
97   and quantification identify the putative binding sites (figure adapted from Figdraw). **c**, RNA-degrading chimeras
98   (RIBOTACs) recruit RNase L at the target RNA to degrade viral RNAs.

99 **Results**

100 **Chemical optimization of the coumarin derivatives for SL5 RNA binding**

101 We previously synthesized a collection of coumarin derivatives that are known to bind to
102 RNAs[31]. Each of these coumarin derivatives is fluorescent (excitation/emission = 400/480 nm),
103 enabling us to use fluorescence polarization (FP) to determine the in vitro binding affinity with
104 the RNA receptors. We in vitro transcribed SL5 RNA (144–303, RefSeq NC_045512) and
105 screened the compound library using the FP assay (Extended Data Fig. 1). **C2** binds to SL5 at a
106 dissociation constant (K_d) of 1.45 µM (Table 1). Elimination of the ethyl substituent on the A ring
107 (**C4**) did not improve the binding affinity to SL5 RNA (Table 1). In contrast, a bulky substituent
108 on the A ring (**C6**) impeded the interaction with SL5 (Table 1). This indicated that a non-
109 sterically hindered linker might be suitable for conjugation on ring A without affecting the ligand
110 binding affinity to SL5 RNA. We found **C29** the best ligand in our compound collection, which
111 binds to SL5 RNA at a K_d of 0.47 µM. Comparing to **C4**, **C29** has a different set of substituents
112 on ring E, and therefore, we further investigated ring E while keep ring A as unsubstituted
113 piperazine (Table 1). In vitro FP assay showed that a fluorinated analog, **C30**, further improves
114 the binding affinity (K_d = 0.22 µM). Changing the F group into Cl (**C32**) or CF_3 (**C36**) groups or
115 alternating the fluorinated site (**C31**) all reduced the binding affinities (Table 1). To our
116 knowledge, **C30** is the strongest small-molecule ligand to the SARS-CoV-2 SL5 RNA.

117 **Table 1. Structure-activity-relationship study of coumarin derivatives for in vitro binding affinities with SL5**
118 **RNA.**
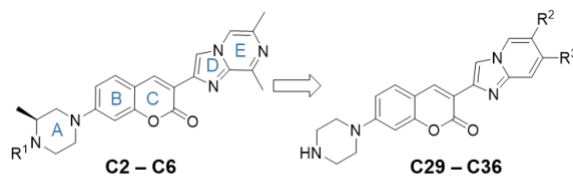
Name	R^1	R^2	R^3	SL5 K_d (µM)
C2	CH$_2$CH$_3$	NA	NA	1.45 ± 0.38
C4	H	NA	NA	1.24 ± 0.29
C6	CH$_2$CH$_2$NHBoc	NA	NA	5.67 ± 4.78
C29	NA	H	H	0.47 ± 0.09
C30	NA	H	F	0.22 ± 0.09
C31	NA	F	H	0.69 ± 0.07
C32	NA	H	Cl	0.42 ± 0.09
C36	NA	H	CF$_3$	1.41 ± 0.25

119

120 cgSHAPE-seq uncovered the bulged G in SL5 as the C30 binding site
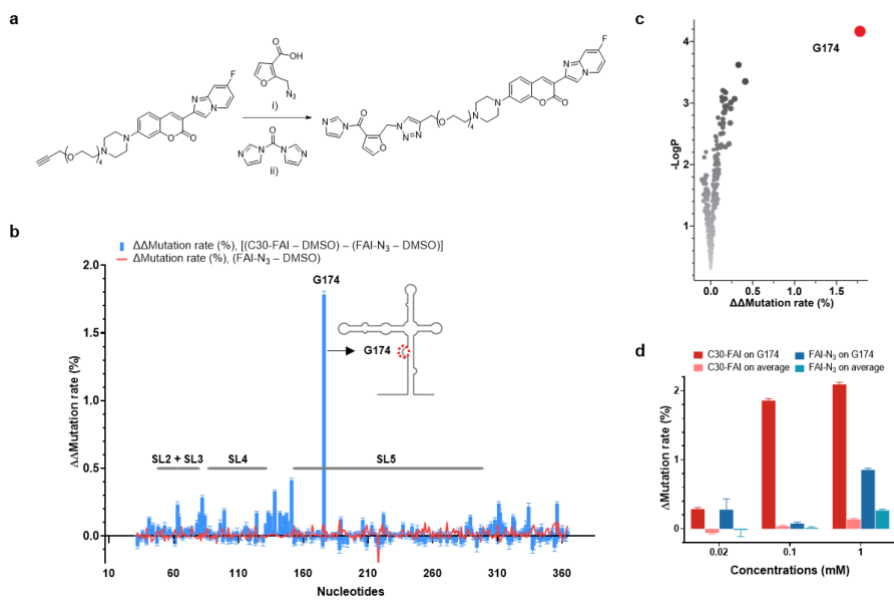121 We were inspired by a commonly used method for RNA structure elucidation called SHAPE and
122 sought to develop a new chemical-guided sequencing-based method to identify the binding site
123 of **C30** in SL5 RNA. We named the new chemical probing method chemical-guided SHAPE
124 sequencing, or cgSHAPE-seq. Conventional SHAPE uses electrophilic reagents that can form
125 ester adducts on the 2'-OH of the ribose. The unpaired nucleotides have higher accessibility for
126 acylation reactions, which is the basis of structure-based differential acylation activity.
127 Therefore, identification of the acylation site would provide information in RNA base-pairing in

128   the conventional SHAPE. Importantly, the electrophile-ribose adduct can create a mutation
129   during reverse transcription (i.e., primer extension). As a result, conventional SHAPE coupled
130   with quantitative mutational profiling has become a gold standard method to explore RNA
131   topology in vitro and in vivo[32–36]. The key advantage of SHAPE is that the electrophile can
132   usually react with all four nucleotides (A, U, G, or C) with similar activity. We wondered if the
133   ribose acylation could be repurposed for identification of small-molecule binding sites by
134   covalently linking electrophile moieties to RNA-binding chemical ligands.

135   First, we selected furoyl acylimidazole (FAI) as the electrophile for synthesizing the chemical
136   probe. Compared to other electrophile moieties such as anhydride and acyl cyanide, FAI is
137   more resistant to hydrolysis with a half-life of 73 min in H_2O[37,38]. The hydrolysis-resistant probe
138   design renders the synthesis and storage less demanding for anhydrous experimental facilities.
139   An azide group on the furoyl moiety was used to provide a click-chemistry handle to conjugate
140   with **C30** (Fig. 2a). After the [3+2] cycloaddition reaction, the carboxylic acid was then converted
141   into an acyl imidazole moiety under a mild condition, finalizing the synthesis of **C30-FAI** probe
142   (Fig. 2a). The acyl imidazole probe was prepared freshly and used directly without further
143   purification (see Method). We tested the reactivity of FAI-N_3 with a denatured RNA and
144   confirmed that FAI-N_3 can react with all four nucleotides and generate SHAPE signal at a high
145   concentration (Extended Data Fig. 2).

146   Next, we applied **C30-FAI** in SARS-CoV-2 5' UTR RNA to elucidate the binding site of **C30**. It is
147   known that conventional SHAPE experiments usually require high concentration (10–100 mM)
148   of acyl imidazole (e.g., FAI) for ribose acylation. To avoid obtaining structure-based differential
149   acylation activity caused by FAI moiety alone, we chose to use a much lower dose of the
150   chemical probe for cgSHAPE-seq. We reasoned that at low concentration of the probe (0.02–1
151   mM), the differential acylation activity would be predominantly caused by ligand binding (i.e.,
152   proximity-promoted acylation). Briefly, the total RNA was extracted from SARS-CoV-2 5' UTR
153   expressing cells (see Method) and refolded in buffer. **C30-FAI**, FAI-N_3, or DMSO was
154   individually reacted with the folded RNA for 15 min at 37 °C. After the reaction, we used
155   ProtoScript II reverse transcriptase (New England Biolabs) in the presence of $MnCl_2$ (3 mM) for
156   primer extension using a protocol modified from the literature report (see Method)[32]. The cDNA
157   was then amplified by PCR in the SARS-CoV-2 5' UTR region and the resulting amplicon was
158   subsequently sequenced. We applied an existing software package ShapeMapper2 developed
159   by the Weeks group for mutational profiling analysis[32,39]. We calculated the background
160   Δmutation rate (FAI-N_3 – DMSO) for each nucleotide and pleasingly observed a low background
161   signal at 0.02 and 0.1 mM of FAI-N_3, indicating that the structure-based differential acylation
162   activity is negligible in cgSHAPE-seq at these concentrations (Extended Data Fig. 3). We then
163   calculated the RNA ligand-induced ΔΔmutation rate [(C30-FAI – DMSO) – (FAI-N_3 – DMSO)] for
164   each nucleotide and identified G174 as the only significantly mutated nucleotides in 0.1 mM
165   probe-treated samples (Fig. 2b,c). In 1 mM probe treated samples, a lower signal-to-noise ratio
166   was observed even though the mutational result also implied the G174 as the primary **C30**
167   binding site (Fig. 2d). At 1 mM, FAI-N3 also significantly increased the Δmutation rate at G174,
168   implying the contribution of structure-based SHAPE activities started to emerge (Fig. 2d).
169   Mapping the nucleotide with previously identified secondary structures uncovered that G174 is a
170   single-nucleotide bulge in the SL5 stem region[8–12].

Fig. 2 | Identification of the binding site by cgSHAPE-seq. a, cgSHAPE-seq probe (**C30-FAI**) synthetic route. Reaction conditions: i) tris(hydroxypropyltriazolylmethyl)amine, $CuSO_4$, sodium ascorbate, DMSO, room temperature; ii) anhydrous DMSO, room temperature. **b**, cgSHAPE-seq mutational profiling analysis of the SL5 sequence in total RNA extract treated with **C30-FAI** (0.1 mM). Δmutation rate ($FAI-N_3$ – DMSO) indicates the background structure-based differential acylation. $\Delta\Delta$mutation rate [(C30-FAI – DMSO) – ($FAI-N_3$ – DMSO)] indicates the proximity-based differential acylation. The cgSHAPE-seq experiments were performed with three replicates (N=3). **c**, Scatter plot of -LogP vs $\Delta\Delta$mutation rate. **d**, Comparison of the Δmutation rates of G174 and on average in RNAs treated with different concentrations of **C30-FAI** or $FAI-N_3$. One data point (C75) was removed as an outlier as it had an abnormally high mutation rate (*Z*-score > 4.0) for the DMSO-treated sample.

We then validated the **C30** binding site in SL5 by testing individual substructures of the SL5 RNA. The loop region of SL5A, SL5B, and a minimized four-helix junction, named SL5^M (containing shorter stems) were synthesized chemically or enzymatically (Fig. 3a). The in vitro binding results demonstrated that only SL5^M retained similar binding affinity to **C30** (Fig. 3a, Extended Data Fig. 4). To further validate the putative binding site G174 in SL5^M, we designed and synthesized SL5^M RNAs with different mutations that disrupt the bulged G or other RNA structures (Fig. 3b). As expected, deletion of G174 or base-pairing G174 with an additional C both resulted in a 7-fold decrease in binding affinity to **C30**. Replacement of G174 with A, C or U also significantly reduced **C30** binding. We also expanded the bulged G by inserting different nucleotides between C173 and U175 or between A270 and G271, all these mutated RNAs were demonstrated 5–6-fold reduced binding affinity to **C30**. These results suggested the importance of a single bulged G in accommodating C30's binding. Changing the closing U-A base pair into C-G (3'-end of G174) or C-G base pair into U-A (5'-end of G174) also resulted in a 4-fold decreased binding. Mutations on other parts of the RNA has less impact (i.e., within 2-fold) in changing the binding affinity to **C30** (Fig. 3b). Altogether, these observations validated that the bulged G region is the primarily binding site in SL5 RNA for **C30**. We concluded that cgSHAPE-seq is a validated method for identifying the binding site of RNA-binding small molecules.

198
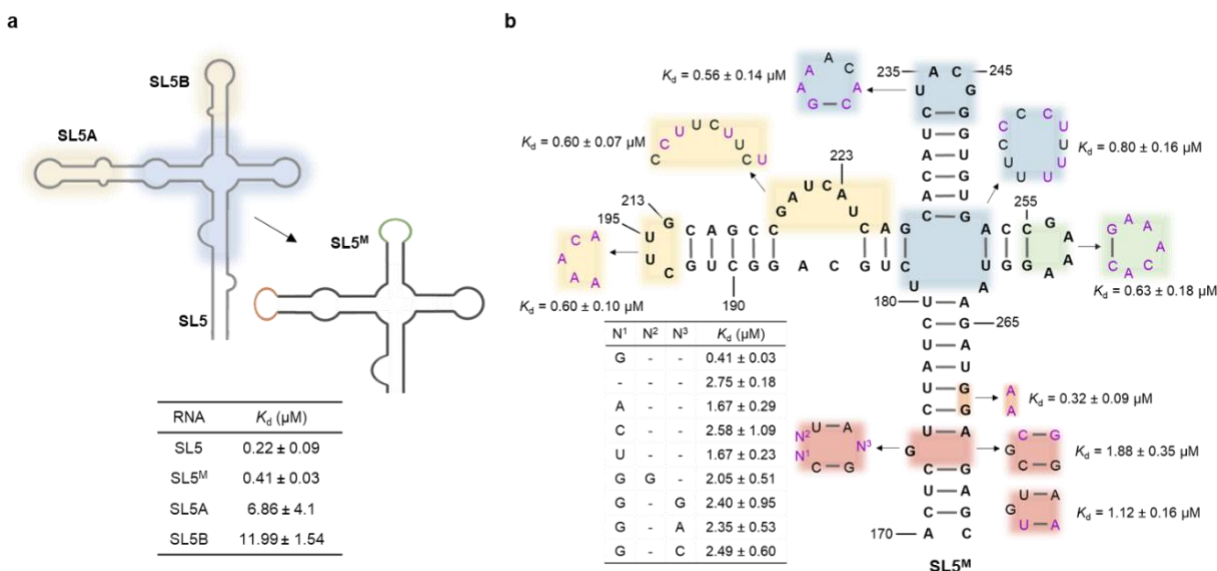
Fig. 3 | Validation of the binding site. a, Structural fragments of SL5 and their binding affinities to **C30**. **b**, SL5^M mutants and their binding affinities to **C30**.

Comparison of two RNase L recruiting moieties in RIBOTACs

We then conjugated **C30** with RLRs to synthesize SL5-targeting RNA degraders (RIBOTACs). Two different conjugation sites were used on rings A and E of **C30**, respectively (Fig. 4a). For RLR conjugation on the A ring, the acylating moiety in the above cgSHAPE probe (**C30-FAI**) was replaced with RLR moieties. We notice that in most reported co-NMR structures of RNA bulges and small molecules that are similar to **C30**, both ends of the small molecules are solvent accessible[40–42]. Therefore, ring E was also explored for conjugation to RLRs. We replaced the electronegative fluorine atom on ring E into an oxygen, which was further used for RLR attachment (Fig. 4a).

For RLR moieties, the natural RNase L ligand 2'-5'-lined oligoadenylate (2-5A) and its synthetic mimic **D1** were both previously reported to be used in RNA-degrading chimeras (Extended Data Fig. 5)[23,24]. Combining the two conjugation sites and two RLR structures, we obtained four RIBOTAC candidates, **C47**, **C48**, **C64**, and **C65**, for SL5 RNA degradation (Fig. 4a). We validated that the polyethylene glycol (PEG) linker on 2-5A does not affect the activity in a reported RNase L degradation assay with a 5' 6-fluorescein-tagged model RNA containing multiple RNase L cleavage sites[43,44] (Extended Data Fig. 5a). It was demonstrated that the binding affinity between RNase L and **D1** ($K_d ≈ 18$ μM) is 80,000-fold weaker than that observed for 2-5A[43]. Consistent with this reported in vitro binding data, the synthetic **D1** alone is > 10,000 times weaker than 2-5A in the in vitro RNase L degradation assay (Extended Data Fig. 5b,c).

Next, we tested the four RIBOTACs in the RNase L degradation assay with purified SL5 RNA and observed their activities in order: **C64** > **C47** ≈ **C48** > **C65** (Fig. 4b, Extended Data Fig. 6a). To our surprise, the RIBOTAC **C64** with **D1** as the RLR moiety is much stronger than **C65** with 2-5A at 50 μM (Fig. 4b). This result is contrary to what we would have predicted based on the activities of the RLR moieties per se. We validated these in vitro findings in SARS-CoV-2 5'

225 UTR expressing 293T cells. In this cell model, the SARS-CoV-2 5' UTR sequence was fused to
226 a CMV promoter-controlled Gaussia luciferase expression cassette (Fig. 4c; for sequences, see
227 Method). Consistent with the RNase L degradation assay result, the maximum potency of **C64**
228 (i.e., RNA reduction level) was significantly better than **C65** (Fig. 4c). The activities of **C47** and
229 **C48** in this cell model are similar, between those of **C64** and **C65** (Extended Data Fig. 6b).

230
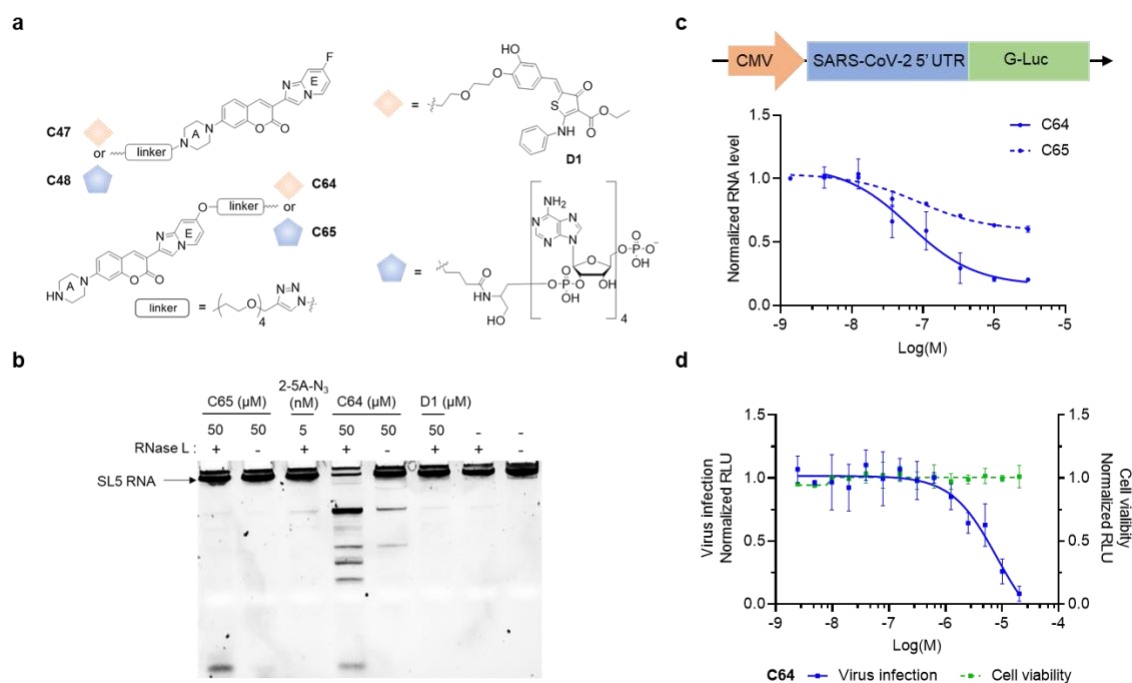
Fig. 4 | RNA degrading activity and anti-viral activity of C30-based RIBOTACs. a, Synthesis of **C30**-based
RIBOTACs using conjugation sites on rings A or E of **C30**. **b**, Comparison of two RLR moieties in the RIBOTAC
modality using the in vitro RNase L degradation assay with purified SL5 RNA. **c**, Cellular activity of RIBOTACs in
SARS-CoV-2 5' UTR expressing cells. **d**, Inhibitory effect of RIBOTAC **C64** in SARS-CoV-2 infected A549 cells. The
cytotoxicity of the compound was also evaluated. The dose-response curves are representative of three independent
measurements (N = 3).

Efficacy of RIBOTAC in live virus infection assay

238 Finally, we tested the activity of **C64** in SARS-CoV-2 infected cells. The SARS-CoV-2 virus was
239 engineered to include a Nano Luciferase (NLuc) reporter by fusing NLuc onto ORF7 of the
240 SARS-CoV-2 genome[45]. In this way, the NLuc signal is proportional to the viral protein copy
241 number in cells. We applied a human lung epithelial carcinoma cell line A549 expressing high
242 level of ACE2 as the host cell[45]. The cells were infected with the SARS-CoV-2-NLuc virus at a
243 multiplicity of infection (MOI) of 2.0 at 1 h before the treatment with RIBOTACs **C64** for 3 d. To
244 our satisfactory, **C64** showed > 95% inhibition at 20 µM (Fig. 4d). At the same concentration, no
245 major toxicity is observed in A549 cells (Fig. 4d).

Discussion
247 cgSHAPE-seq has several potential limitations in application. For example, the FAI-based
248 probes used in this report would not be compatible with strong nucleophilic RNA ligands[14] due
249 to self-reaction. In addition, as shown in conventional SHAPE, FAI moiety has a higher reactivity

250   towards unpaired RNA nucleotides. Although most of reported RNA ligands targets the unpaired
251   region[46,47], cgSHAPE-seq may be less reactive for ligands that binds to the double-stranded
252   RNA grooves. Finally, in our model denatured RNA, FAI-N_3 react with all four nucleotides.
253   However, the reactivity of FAI-N_3 and A, U, G, and C are not equal. In this model, we found FAI-
254   N_3 has a higher reactivity bias towards G and against U (Extended Data Fig. 2). For this reason,
255   the cgSHAPE activities on G and U might be over- and under-estimated, respectively.

256   In our cgSHAPE-seq result, apart from G174, we also observed a cluster of nucleotides from
257   A131 to G149 showing slightly higher mutation rate than others (Fig. 2c). This can be potentially
258   caused by the nonspecific binding of **C30** with flexible sequence[31]. RNA targeting strategies are
259   known to have off-target effects due to shallow binding sites on RNAs and relatively weak
260   binding affinity for small molecules. **C64** at 3 µM can cause 13 gene down regulation
261   (log2FoldChange < −2) and > 23 gene upregulation (log2FoldChange > 2) in the transcriptome
262   (Extended Data Fig. 7, Supplementary Table S1). The activity of the RIBOTAC might be
263   improved if a more potent and selective RNase L recruiter is used[48]. Specifically, we showed
264   that the natural RNase L recruiter/activator 2-5A, which is negatively charged, is sometimes not
265   compatible with the positively charged RNA binder **C30** (Fig. 4b). For this reason, new synthetic
266   RNase L recruiter should probably be considered to be neutral or positively charged as most of
267   the reported RNA ligands are also positively charged[49–51].

268   In summary, we developed a new generalizable chemical probing method called cgSHAPE-seq
269   for quickly identifying small molecule-RNA binding sites by sequencing. cgSHAPE probes react
270   with the 2'-OH groups on the ribose close to the binding sites with a mitigated dependency of
271   the nucleobase identity observed in other reported methods. We used cgSHAPE-seq to identify
272   a bulged G on SL5 as the primary binding site on the SARS-CoV-2 5' UTR targeted by the
273   newly discovered coumarin derivative **C30**. Finally, we developed a novel **C30**-based RNA
274   degrader (RIBOTAC) capable of degrading viral RNA transcripts in cells and inhibiting virus
275   replication in SARS-CoV-2 infected cells, offering crucial insights into RNA degrading chimeras'
276   design.

277   **References**
278   1.   Hegde, S., Tang, Z., Zhao, J. & Wang, J. Inhibition of SARS-CoV-2 by Targeting
279   Conserved Viral RNA Structures and Sequences. *Front. Chem.* **9**, 802766 (2021).

280   2.   Wu, F. *et al.* A new coronavirus associated with human respiratory disease in China.
281   *Nature* **579**, 265–269 (2020).

282   3.   Malone, B., Urakova, N., Snijder, E. J. & Campbell, E. A. Structures and functions of
283   coronavirus replication-transcription complexes and their relevance for SARS-CoV-2 drug
284   design. *Nat. Rev. Mol. Cell Biol.* **23**, 21–39 (2022).

285   4.   de Breyne, S. *et al.* Translational control of coronaviruses. *Nucleic Acids Research* vol.
286   48 12502–12522 (2020).

287   5.   Zúñiga, S., Sola, I., Alonso, S. & Enjuanes, L. Sequence motifs involved in the regulation
288   of discontinuous coronavirus subgenomic RNA synthesis. *J. Virol.* **78**, 980–94 (2004).

289   6.   Sola, I., Almazán, F., Zúñiga, S. & Enjuanes, L. Continuous and Discontinuous RNA
290   Synthesis in Coronaviruses. *http://dx.doi.org/10.1146/annurev-virology-100114-055218* **2**,
291   265–288 (2015).

292   7.   Escors, D., Izeta, A., Capiscol, C. & Enjuanes, L. Transmissible Gastroenteritis
293   Coronavirus Packaging Signal Is Located at the 5′ End of the Virus Genome. *J. Virol.* **77**,
294   7890–7902 (2003).

295   8.   Zhao, J., Qiu, J., Aryal, S., Hackett, J. L. & Wang, J. The RNA Architecture of the SARS-
296   CoV-2 3′-Untranslated Region. *Viruses* **12**, 1473 (2020).

297   9.   Sun, L. *et al.* In vivo structural characterization of the SARS-CoV-2 RNA genome
298   identifies host proteins vulnerable to repurposed drugs. *Cell* **184**, 1865-1883.e20 (2021).

299   10. Huston, N. C. *et al.* Comprehensive in vivo secondary structure of the SARS-CoV-2
300   genome reveals novel regulatory motifs and mechanisms. *Mol. Cell* **81**, 584-598.e5
301   (2021).

302   11. Manfredonia, I. *et al.* Genome-wide mapping of SARS-CoV-2 RNA structures identifies
303   therapeutically-relevant elements. *Nucleic Acids Res.* (2020) doi:10.1093/nar/gkaa1053.

304   12. Sanders, W. *et al.* Comparative analysis of coronavirus genomic RNA structure reveals
305   conservation in SARS-like coronaviruses. *bioRxiv Prepr. Serv. Biol.* (2020)
306   doi:10.1101/2020.06.15.153197.

307   13. Lan, T. C. T. *et al.* Structure of the full SARS-CoV-2 RNA genome in infected cells.
308   *bioRxiv* (2020) doi:10.1101/2020.06.29.178343.

309   14. Zafferani, M. *et al.* Amilorides inhibit SARS-CoV-2 replication in vitro by targeting RNA
310   structures. *Sci. Adv.* **7**, eabl6096 (2021).

311   15. Velagapudi, S. P. *et al.* Defining RNA-Small Molecule Affinity Landscapes Enables
312   Design of a Small Molecule Inhibitor of an Oncogenic Noncoding RNA. *ACS Cent. Sci.* **3**,
313   205–216 (2017).

314   16. Suresh, B. M. *et al.* A general fragment-based approach to identify and optimize bioactive
315   ligands targeting RNA. *Proc. Natl. Acad. Sci. U. S. A.* **117**, 33197–33203 (2020).

316   17. Velagapudi, S. P. *et al.* Design of a small molecule against an oncogenic noncoding
317   RNA. *Proc. Natl. Acad. Sci. U. S. A.* **113**, 5898–903 (2016).

318   18. Velagapudi, S. P., Li, Y. & Disney, M. D. A cross-linking approach to map small molecule-
319   RNA binding sites in cells. *Bioorganic Med. Chem. Lett.* **29**, 1532–1536 (2019).

320   19. Guan, L. & Disney, M. D. Covalent Small-Molecule-RNA Complex Formation Enables
321   Cellular Profiling of Small-Molecule-RNA Interactions. *Angew. Chemie Int. Ed.* **52**,
322   10010–10013 (2013).

323   20. Mukherjee, H. *et al.* PEARL-seq: A Photoaffinity Platform for the Analysis of Small

324   Molecule-RNA Interactions. *ACS Chem. Biol.* **15**, 2374–2381 (2020).

325   21.   Balaratnam, S. *et al.* A chemical probe based on the PreQ1 metabolite enables
326   transcriptome-wide mapping of binding sites. *Nat. Commun.* **12**, 5856 (2021).

327   22.   Torrence, P. F. *et al.* Targeting RNA for degradation with a (2'-5')oligoadenylate-
328   antisense chimera. *Proc. Natl. Acad. Sci. U. S. A.* **90**, 1300–4 (1993).

329   23.   Haniff, H. S. *et al.* Targeting the SARS-CoV-2 RNA Genome with Small Molecule Binders
330   and Ribonuclease Targeting Chimera (RIBOTAC) Degraders. *ACS Cent. Sci.* **6**, 1713–
331   1721 (2020).

332   24.   Costales, M. G., Matsumoto, Y., Velagapudi, S. P. & Disney, M. D. Small Molecule
333   Targeted Recruitment of a Nuclease to RNA. *J. Am. Chem. Soc.* **140**, 6741–6744 (2018).

334   25.   Costales, M. G., Suresh, B., Vishnu, K. & Disney, M. D. Targeted Degradation of a
335   Hypoxia-Associated Non-coding RNA Enhances the Selectivity of a Small Molecule
336   Interacting with RNA. *Cell Chem. Biol.* **26**, 1180-1186.e5 (2019).

337   26.   Costales, M. G. *et al.* Small-molecule targeted recruitment of a nuclease to cleave an
338   oncogenic RNA in a mouse model of metastatic cancer. *Proc. Natl. Acad. Sci.* **117**, 2406–
339   2411 (2020).

340   27.   Liu, X. *et al.* Targeted Degradation of the Oncogenic MicroRNA 17-92 Cluster by
341   Structure-Targeting Ligands. *J. Am. Chem. Soc.* **142**, 6970–6982 (2020).

342   28.   Su, X. *et al.* Efficient Inhibition of SARS-CoV-2 Using Chimeric Antisense
343   Oligonucleotides through RNase L Activation*. *Angew. Chem. Int. Ed. Engl.* **60**, 21662–
344   21667 (2021).

345   29.   Zhang, P. *et al.* Reprogramming of Protein-Targeted Small-Molecule Medicines to RNA
346   by Ribonuclease Recruitment. *J. Am. Chem. Soc.* **143**, 13044–13055 (2021).

347   30.   Bush, J. A. *et al.* Ribonuclease recruitment using a small molecule reduced c9ALS/FTD
348   r(G4C2) repeat expansion in vitro and in vivo ALS models. *Sci. Transl. Med.* **13**,
349   eabd5991 (2021).

350   31.   Tang, Z. *et al.* Recognition of single-stranded nucleic acids by small-molecule splicing
351   modulators. *Nucleic Acids Res.* **49**, 7870-7883. PMC8373063 (2021).

352   32.   Smola, M. J., Rice, G. M., Busan, S., Siegfried, N. A. & Weeks, K. M. Selective 2 ' -
353   hydroxyl acylation analyzed by primer extension and mutational profiling (SHAPE-MaP)
354   for direct , versatile and accurate RNA structure analysis. *Nat. Protoc.* **10**, 1643–1669
355   (2015).

356   33.   Weeks, K. M. & Mauger, D. M. Exploring RNA Structural Codes with SHAPE Chemistry.
357   *Acc. Chem. Res.* **44**, 1280–1291 (2011).

358   34.   Siegfried, N. A., Busan, S., Rice, G. M., Nelson, J. A. E. & Weeks, K. M. RNA motif

359   discovery by SHAPE and mutational profiling (SHAPE-MaP). *Nat. Methods* **11**, 959
360   (2014).

361 35. Spitale, R. C. *et al.* Structural imprints in vivo decode RNA regulatory mechanisms.
362   *Nature* **519**, 486–490 (2015).

363 36. Flynn, R. A. *et al.* Transcriptome-wide interrogation of RNA secondary structure in living
364   cells with icSHAPE. *Nat. Protoc.* **11**, 273–290 (2016).

365 37. Spitale, R. C. *et al.* RNA SHAPE analysis in living cells. *Nat. Chem. Biol.* **9**, 18–20 (2013).

366 38. Chan, D., Beasley, S., Zhen, Y. & Spitale, R. C. Facile synthesis and evaluation of a dual-
367   functioning furoyl probe for in-cell SHAPE. *Bioorg. Med. Chem. Lett.* **28**, 601–605 (2018).

368 39. Busan, S. & Weeks, K. M. Accurate detection of chemical modifications in RNA by
369   mutational profiling (MaP) with ShapeMapper 2. *RNA* **24**, 143–148 (2018).

370 40. Campagne, S. *et al.* Structural basis of a small molecule targeting RNA for a specific
371   splicing correction. *Nat. Chem. Biol. 2019 1512* **15**, 1191–1198 (2019).

372 41. Nagano, K., Kamimura, T. & Kawai, G. Interaction between a fluoroquinolone derivative
373   and RNAs with a single bulge. *J. Biochem.* **171**, 239–244 (2022).

374 42. Ichijo, R., Kamimura, T. & Kawai, G. Interaction between a fluoroquinolone derivative
375   KG022 and RNAs: Effect of base pairs 3′ adjacent to the bulged residues. *Front. Mol.*
376   *Biosci.* **10**, 168 (2023).

377 43. Thakur, C. S. *et al.* Small-molecule activators of RNase L with broad-spectrum antiviral
378   activity. *Proc. Natl. Acad. Sci. U. S. A.* **104**, 9585–90 (2007).

379 44. Thakur, C. S., Xu, Z., Wang, Z., Novince, Z. & Silverman, R. H. A convenient and
380   sensitive fluorescence resonance energy transfer assay for RNase L and 2',5'
381   oligoadenylates. *Methods Mol. Med.* **116**, 103–13 (2005).

382 45. Adhikary, P. *et al.* Discovery of Small Anti-ACE2 Peptides to Inhibit SARS-CoV-2
383   Infectivity. *Adv. Ther.* **4**, 2100087 (2021).

384 46. Hargrove, A. E. Small molecule–RNA targeting: starting with the fundamentals. *Chem.*
385   *Commun.* **56**, 14744–14756 (2020).

386 47. Childs-Disney, J. L. *et al.* Targeting RNA structures with small molecules. *Nat. Rev. Drug*
387   *Discov.* **21**, 736–762 (2022).

388 48. Meyer, S. M. *et al.* DNA-Encoded Library Screening To Inform Design of a Ribonuclease
389   Targeting Chimera (RiboTAC). *J. Am. Chem. Soc.* **144**, 21096–21102 (2022).

390 49. Morgan, B. S., Forte, J. E., Culver, R. N., Zhang, Y. & Hargrove, A. E. Discovery of Key
391   Physicochemical, Structural, and Spatial Properties of RNA-Targeted Bioactive Ligands.
392   *Angew. Chemie - Int. Ed.* **56**, 13498–13502 (2017).

393 50. Velagapudi, S. P., Gallo, S. M. & Disney, M. D. Sequence-based design of bioactive
394   small molecules that target precursor microRNAs. *Nat. Chem. Biol.* **10**, 291–297 (2014).

395 51. Disney, M. D. *et al.* Informa 2.0: A Platform for the Sequence-Based Design of Small
396   Molecules Targeting Structured RNAs. *ACS Chem. Biol.* **11**, 1720–1728 (2016).

397

Methods
Synthesis of C30-FAI (cgSHAPE probe)

400 Compound **C30-alkyne** (50 mg, 0.08 mmol) in DMSO (1 mL) was added 2-(azidomethyl)furan-
401 3-carboxylic acid (15 mg, 0.09 mmol), THPTA (9 mg, 0.02 mmol), sodium ascorbate (8 mg, 0.04
402 mmol) and $CuSO_4$ (3 mg, 0.02 mmol). The reaction vial was sealed, evacuated, and refilled with
403 N_2 three times and stirred at room temperature for overnight. DMSO was removed under
404 vacuum and the residue was purified by silica gel column chromatography (0 – 10% CH_3OH in
405 CH_2Cl_2) to afford **C30-FCA** as a yellow solid (45 mg, 70%). MS-ESI (*m/z*) [M+1]$^+$ 746.28.

406 ^1H NMR (500 MHz, DMSO-d_6) δ 8.71 – 8.68 (m, 2H), 8.52 (s, 1H), 8.09 (s, 1H), 7.71 – 7.68 (m,
407 2H), 7.38 (dd, *J* = 10.1, 2.6 Hz, 1H), 7.02 (dd, *J* = 9.0, 2.3 Hz, 1H), 6.97 (td, *J* = 7.6, 2.6 Hz, 1H),
408 6.88 (d, *J* = 2.4 Hz, 1H), 6.72 (d, *J* = 1.9 Hz, 1H), 5.92 (s, 2H), 4.52 (s, 2H), 3.58 – 3.51 (m,
409 14H), 3.38 (t, *J* = 5.1 Hz, 4H), 2.59 (t, *J* = 5.1 Hz, 4H), 2.56 (t, *J* = 5.8 Hz, 2H).

410 ^{13}C NMR (126 MHz, DMSO-d_6) δ 160.2 (d, *J* = 252 Hz), 159.5, 154.9, 153.3, 152.2, 144.4,
411 144.3, 143.4, 139.4, 138.6, 129.6, 129.2 (d, *J* = 11.8 Hz), 124.2, 114.5, 112.1, 111.7, 111.4,
412 110.2, 104.2 (d, *J* = 29.8 Hz), 99.6, 99.4, 69.8, 69.7, 69.1, 63.4, 57.0, 54.9, 52.6, 46.7, 44.8.

413 Compound **C30-FCA** (45 mg, 0.06 mmol) in anhydrous DMSO (0.6 mL) was added
414 carbonyldiimidazole (CDI, 10 mg, 0.06 mmol) and the reaction mixture was stirred at room
415 temperature for 1 h. The reaction mixture contains ~75% **C30-FAI** and ~25% unreacted **C30-**
416 **FCA** (see Supplementary Information) and was used directly in RNA modification. The stock
417 solution was used as a **75 mM** and can be stored at –80 °C for long-term storage.

cgSHAPE-seq using Total RNA Extract from Cells

419 SARS-CoV-2 5' UTR expressing cells were harvested and pelleted. Total RNA was extracted
420 using TRIzol Reagent (Invitrogen) per the user's manual. An on-column DNA digestion was
421 performed to remove the residual genomic DNA in total RNA using DNase I (10 U/μL, Roche)
422 and RDD buffer (Qiagen). Purified total RNA was dissolved in water and stored at –80 °C before
423 use. For RNA modification, 5 μg total RNA was used for each reaction. **C30-FAI** and FAI-N_3
424 were prepared at 20 mM, 2 mM, and 0.4 mM in DMSO as 20✕ working solution. Briefly, total
425 RNA was added water and 5✕ folding/reaction buffer (500 mM HEPES pH 7.4, 500 mM KCl, 30
426 mM $MgCl_2$) to make a 47.5 μL solution. The solution was incubated at 37 °C for 30 min to refold.
427 2.5 μL **C30-FAI** (cgSHAPE probe), FAI-N_3 (background control) or DMSO was added to the
428 total RNA and mix well by pipetting. The mixture was incubated at 37 °C for 15 min and then
429 quenched by adding RLT buffer (Qiagen). The RNA was then extracted using RNeasy kit

430 (Qiagen). 500 ng total RNA was used for reverse transcription and then PCR as described
431 below. All reactions were performed in triplicates.

432 For reverse transcription (10 μL reaction), probe or DMSO treated RNA and reverse
433 transcription primer (0.5 μM in final reaction buffer) were heated at 70 °C for 5 min and snap-
434 cooled on ice for 1min. 5× reaction buffer (375 mM Tris-HCl, 500 mM KCl, 15 mM MnCl$_2$, pH
435 7.4, 2 μL), DTT (100 mM, 1 μL), dNTP (10 mM, 0.5 μL), ProtoScript II (0.5 μL, New England
436 Biolabs, M0368L) and RNase inhibitor (0.2 μL, ApexBio, K1046) were added. The reaction was
437 incubated at 42 °C for 1 h and deactivated at 70 °C for 15 min. In each PCR reaction (50 μL),
438 cDNA (2.5 μL) was mixed with Phire Hot Start II DNA Polymerase (Thermo Fisher, 1 μL), dNTP
439 (10 mM, 1 μL), 5× Phire Green reaction buffer (10 μL), primers (0.5 μM in final reaction buffer)
440 and water (35.5 μL). After reaction, the amplicon was purified using a DNA Clean &
441 Concentrator kit (Zymo Research) following user's manual. The purified DNA was submitted for
442 next-generation sequencing (Amplicon-EZ, Azenta Life Sciences).

443 An integrated software package developed by Busan and Weeks, ShapeMapper2 was used to
444 analyze the fastq files for mutational profiling and the rresult was used to generate Figures 2b,
445 2c, and Extended Data Fig. 3[39]. The reference sequence (SARS-CoV-2_5_UTR.fa) required for
446 ShapeMapper2 is listed below.

447 >SARS-CoV-2_5_UTR

448 aggtttataccttcccaggtaacAAACCAACCAACTTTCGATCTCTTGTAGATCTGTTCTCTAAACGAAC
449 TTTAAAATCTGTGTGGCTGTCACTCGGCTGCGTGCTTAGTGCACTCACGCAGTATAATTAAT
450 AACTAATTACTGTCGTTGACAGGACACGAGTAACTCGTCTATCTTCTGCAGGCTGCTTACG
451 GTTTCGTCCGTGTTGCAGCCGATCATCAGCACATCTAGGTTTCGTCCGGGTGTGACCGAAA
452 GGTAAGATGGAGAGCCTTGTCCCTGGTTTCAACGAGGGAGTCAAAGTTCTGTTTGCCCTGA
453 TCTGCATCGCTGTGGCCGAGGCCAAGCCCACCGAGAACAACGAagacttcaacatcgtggccg.
454 (lowercase = primer binding sequences).

455

In Vitro RNase L Degradation Assay

457 Purified recombinant GST-tagged RNase L was purchased from MyBioSource (MBS1041064).
458 The buffer of RNase L was exchanged into a buffer containing 50 mM Tris-HCl (pH 7.4) and 100
459 mM NaCl using Zeba Desalting Column (Thermo Fisher, 8766) using the manufacturer's
460 protocol. For RNase L degradation of SL5 RNA, T7 transcribed SL5 RNA was first purified by
461 polyacrylamide gel electrophoresis (PAGE) and recovered using small-RNA PAGE Recovery Kit
462 (Zymo Research, R1070)**.** RNase L (1.3 μg in 5 μL) was incubated in the presence of **C47**, **C48**,
463 **C64**, **C65**, or DMSO control in the cleavage buffer (final reaction volume is 8 μL) at 4 °C for 12
464 h. The 1X cleavage buffer contains 25 mM Tris-HCl (pH 7.4), 10 mM MgCl$_2$, 100 mM KCl, 50
465 μM ATP, and 7 mM β-mercaptoethanol. The SL5 RNA (120 ng in 2 μl H$_2$O) was then added into
466 the reaction mixture and incubated for another 2 h at 22 °C. The reaction was stopped by
467 adding RNA Gel Loading Dye (Thermo Fisher, R0641) at 1:1 ratio. The samples (4 μl) were
468 then loaded on TBE-urea polyacrylamide gel (20%) for electrophoresis (180 V for 85 min). The

469   gel was stained with SYBR safe (1/50,000, ApexBio, A8743) in TBE buffer for 1 min and

470   visualized on gel imager (Thermo Fisher, iBright FL1500).

471   The RNA sequence of SL5 used in this assay is: 5'-

472   UCGUUGACAGGACACGAGUAACUCGUCU

473   AUCUUCUGCAGGCUGCUUACGGUUUCGUCCGUGUUGCAGCCGAUCAUCAGCACAUCUA

474   GGUUUCGUCCGGGUGUGACCGAAAGGUAAGAUGGAGAGCCUUGUCCCUGGUUUCAACG

475   A.

476   For RNase L degradation of a model 6-FAM-tagged RNA, RIBOTACs in the above protocol

477   were replaced with **D1** (0.37 µg in 0.75 µl DMSO) or **2-5A-N₃** (0.12 ng in 0.75 µl H_2O)[43,44]. After

478   electrophoresis, the gel was not stained and was directly visualized on the gel imager at the 6-

479   FAM fluorescence channel. The 6-FAM RNA (5'-6-FAM-

480   UUAUCAAAUUCUUAUUUGCCCCAUU

481   UUUUUGGUUUA-BHQ) was purchased from IDT.

482

SARS-CoV-2 5' UTR Expressing Stable Cell Line

484   293T cells (Thermo Fisher, R70007) were cultured in DMEM growth medium (Gibco, 11995040)

485   supplemented with 10% FBS (Cytiva, SH30910.03) and 1% Antibiotic-Antimycotic (Gibco,

486   15240062) at 37 °C in 5% CO_2 atmosphere. For producing the lentivirus, 293T cells were

487   seeded in a 6-well plate (Fisher, FBO12927) at 3 x 10^5 cells per well and transfected with 1 µg

488   of SARS-CoV-2 5' UTR expressing lentivirus vector (pLV-SARS-CoV-2-5'UTR-GLuc) along with

489   the packaging plasmids pMD2.G (0.4 µg) and psPAX2 (0.6 µg) using Lipofectamine 2000

490   (Invitrogen, 11668019). At 24 h post-transfection, the cell medium was replaced with fresh

491   growth medium. 48 h after the change of media, the supernatant containing the lentivirus

492   particles was siphoned and centrifuged at 500 g for 10 min at 4 °C to remove the cell debris.

493   The virus particles were further concentrated at 10X in volume using Lenti-X-concentrator

494   (Clontech, PT4421-2) according to the manufacturer's protocol. The lentivirus can be quantified

495   using literature method[52]. Usually, 10^7–10^8 plaque forming units (pfu)/mL lentivirus was obtained

496   after the concentrator treatment. For lentiviral transduction, 293T cells were inoculated with the

497   concentrated viral suspension (multiplicity of infection ~10) using polybrene (Sigma-Aldrich, TR-

498   1003-G) at a final concentration of 8 µg/mL. At 24 h post-transduction, the culture medium was

499   replaced with fresh growth media. After recovery for 24 h, the transduced cells were then

500   selected in blasticidin (10 µg/mL, Invivogen, ant-bl) for 2 weeks. For stable single clone

501   selection, the cells were diluted in the growth medium containing blasticidin (10 µg/mL) to a final

502   density of 1 cell per 100 µL. The diluted cell suspension was then dispensed to a 96-well plate

503   (100 µL per well). The plate was incubated at 37 °C for 4 weeks. A single cell colony from one

504   of the wells was then selected for experiments.

505   pLV-SARS-CoV-2-5UTR-Luc was constructed by inserting the SARS-CoV-2 5' UTR and

506   Gaussian luciferase into the pLV vector, under the control of the CMV promoter. The insert

507   sequence is as follows:

508 attaaaggtttataccttcccaggtaacaaaccaaccaactttcgatctcttgtagatctgttctctaaacgaactttaaaatctgtgtggctg

509 tcactcggctgcgtgcttagtgcactcacgcagtataattaataactaattactgtcgttgacaggacacgagtaactcgtctatcttctgc

510 aggctgcttacggtttcgtccgtgttgcagccgatcatcagcacatctaggtttcgtccgggtgtgaccgaaaggtaag<u>atg</u>gagagcct

511 tgtccctggtttcaacgagggagtcaaagttctgtttgccctgatctgcatcgctgtggccgaggccaagcccaccgagaacaacgaa

512 gacttcaacatcgtggccgtggccagcaacttcgcgaccacggatctcgatgctgaccgcgggaagttgcccggcaagaagctgcc

513 gctggaggtgctcaaagagatggaagccaatgcccggaaagctggctgcaccaggggctgtctgatctgcctgtcccacatcaagt

514 gcacgcccaagatgaagaagttcatcccaggacgctgccacacctacgaaggcgacaaagagtccgcacagggcggcataggc

515 gaggcgatcgtcgacattcctgagattcctgggttcaaggacttggagcccatggagcagttcatcgcacaggtcgatctgtgtgtgga

516 ctgcacaactggctgcctcaaagggcttgccaacgtgcagtgttctgacctgctcaagaagtggctgccgcaacgctgtgcgacctttg

517 ccagcaagatccagggccaggtggacaagatcaagggggccggtggtgactaa (lowercase = SARS-CoV-2 5'

518 UTR; uppercase = Gaussia luciferase; underline = start codon).

519

Quantitative Reverse Transcription PCR (RT-qPCR) Assay

521 The SARS-CoV-2 5' UTR expressing cells were seeded at 3 x 10^5 cells per well in 12-well

522 plates in 1 mL growth medium at 37 °C for 3 h. The cells were then treated with the compounds

523 (**C47**, **C48**, **C64**, or **C65**) at various concentrations (1.3 nM–3 µM) for 48 h. After treatment, the

524 supernatant was aspirated from each well and the total RNA was then extracted from the cells

525 using RNeasy mini kit (Qiagen, 74104). The total RNAs were quantified by ultraviolet absorption

526 at 260 nm (Thermo Fisher, NanoDrop 1000). Usually 10–20 µg total RNA was obtained from

527 each well. cDNAs were synthesized from 500 ng of total RNA for each sample using M-MLV

528 reverse transcriptase (Promega, M1701) and $(dT)_{25}$ according to the manufacturer's protocol. 1

529 µl of cDNA mixture was used in a 15 µl RT-qPCR reaction (Apex-Bio, K1070). The human

530 GAPDH RNA level was used as the reference for normalization. The RT-qPCR primer

531 sequences used for the PCR are shown below:

532 SL5-SYBR-FW: 5'-CGTTGACAGGACACGAGTAA

533 SL5-SYBR-RV: 5'-TTGAAACCAGGGACAAGGCTC

534 GAPDH-FW: 5'-GACAAGGCTGGGGCTCATTT

535 GAPDH-RV: 5'-CAGGACGCATTGCTGATGAT

536

SARS-CoV-2 Inhibition Assay

538 Vero-E6 cells (ATCC® CRL-1586™) and A549 cells (ATCC® CCL-185) were cultured in

539 Dulbecco's modified Eagle's medium (DMEM, Cytiva Life Science, SH30022) with addition of

540 10% fetal bovine serum (FBS, Millipore Sigma, F0926) at 37°C under 5% CO_2 atmosphere.

541 A549 cells were transduced with a human ACE2-expressing lentivirus vector, and the

542 transduced were cultured in the DMEM plus 2 µg/µL puromycin[45].

543 *Virus and titration*

544   SARS-CoV-2-Nluc was created by engineering the nanoluciferase (Nluc) gene into the OFR7 of

545   the SARS-CoV-2 genome. The insertion site of Nluc at ORF7 was based on previous

546   mNeonGreen reporter SARS-CoV-2[53]. The virus was propagated in Vero-E6 cells once,

547   aliquoted in DMEM, and stored at –80˚C. A biosafety protocol to work on SARS-CoV-2 in the

548   BSL3 Lab was approved by the Institutional Biosafety Committee of the University of Kansas

549   Medical Center.

550   *Plaque assay[54,55]*

551   Vero-E6 cells were seeded in 24-well plates at a density of 0.5×10^6 cells per well. A virus stock

552   was serially diluted at 10-fold in Dulbecco's phosphate-buffered saline, pH7.4 (DPBS). 200 μL of

553   the diluent were added to each well and incubated for 1 h on a rocking rotator. After removing

554   the virus diluent, 0.5 mL of overlay media (1% methylcellulose in DMEM with 5% FBS) were

555   added to each well. The plates were incubated at 37 °C under 5% CO_2 for 4 days. The

556   methylcellulose overlays were aspirated, and the cells were fixed with 10% formaldehyde

557   solution for 30 min and stained with 1% crystal violet solution followed by extensive washing.

558   Plaques in each well were counted and multiplied by the dilution factor to determine the virus

559   titer at pfu/mL.

560   *Determination of half-maximal inhibitory concentration (IC_{50})[45,56]*

561   ACE2-A549 cells were seeded into 96 well plates. When the cells were confluent, SARS-CoV-2-

562   NLuc viruses were diluted with cold PBS and added into each well at a multiplicity of infection

563   (MOI) of 2 (2 pfu/cell). The plates were kept in the CO_2 incubator for 1 hour. Compound **C64**

564   was diluted at 2 x serials from 20 μM to 0.002 μM. The virus-PBS solution was aspirated. Each

565   well was washed with cold PBS three times, and was loaded with the diluted compounds. Each

566   concentration was loaded in triple wells in the plates, and the total volume of each well was 0.2

567   mL. The plates were kept in the incubator. After 3 days post-infection, the culture media were

568   aspirated from each well and the wells were washed with PBS for three times. The nano-

569   luciferase activity assay (Promega, N1110) was carried out by following the manufacturer's

570   instructions. Briefly, 100 ul of cell lysis buffer were added to each well for 10 minutes to

571   completely lyse the cells. Then 100 ul of nano-luciferase reaction reagent were add to each well

572   and the luminescent signal was determined at A490 absorbance on a plate reader (Bio-Tek,

573   Synergy). The IC_{50} was calculated using GraphPad Prism 8.0 software.

574

Statistical Analysis

576   All data shown as means ± s.d. with sample size (N) listed for each experiment. Statistical

577   analysis was carried out with Prism GraphPad 8.0. Unpaired two-sample t-tests were used to

578   analyze significant differences between the group means. The P values were calculated by

579   Prism GraphPad 8.0 or R. For data generated from ShapeMapper2, the standard error (stderr)

580   associated with the mutation rate at a given nucleotide in the S (probe treated) or U (DMSO

581 treated) samples was calculated as: stderr = $\sqrt{mutation\ rate}/\sqrt{reads}$. The standard error of the

582 Δmutation rate at a given nucleotide is: $\sqrt{stderr_S{}^2 + stderr_U{}^2}$.

583

Data Availability

585 The cgSHAPE-seq data for **C30-FAI**, FAI-N$_3$ or DMSO-treated total RNAs, and RNA-seq data
586 for **C64**-treated cells were deposited in NCBI SRA with accession numbers PRJNA950557 and
587 PRJNA947619, respectively.

588

References

590 52.   Barczak, W., Suchorska, W., Rubiś, B. & Kulcenty, K. Universal Real-Time PCR-Based
591 Assay for Lentiviral Titration. *Mol. Biotechnol.* **57**, 195–200 (2015).

592 53.   Xie, X. *et al.* A nanoluciferase SARS-CoV-2 for rapid neutralization testing and screening
593 of anti-infective drugs for COVID-19. *Nat. Commun.* **11**, 5214 (2020).

594 54.   Hao, S. *et al.* Long-term modeling of SARS-CoV-2 infection of in vitro cultured polarized
595 human airway epithelium. *MBio* **11**, 1–17 (2020).

596 55.   Zou, W. *et al.* The sars-cov-2 transcriptome and the dynamics of the s gene furin
597 cleavage site in primary human airway epithelia. *MBio* **12**, (2021).

598 56.   Hao, S. *et al.* Establishment of a Replicon Reporter of the Emerging Tick-Borne Bourbon
599 Virus and Use It for Evaluation of Antivirals. *Front. Microbiol.* **11**, 2229 (2020).

600

Acknowledgments

614

Author contributions

616 J.W. conceived the work. J.W., Z.T., S. Hegde and J.Q. wrote the paper. Z.T and M.S.
617 performed chemical synthesis. Z.T. and J.W. conducted the RNA sequencing and analysis. S.
618 Hegde collected RNA degradation data in vitro and in cells. S. Hao and J.Q. performed the live
619 virus assay.

620

Competing interests

622 The authors declare no competing interests.

623

624
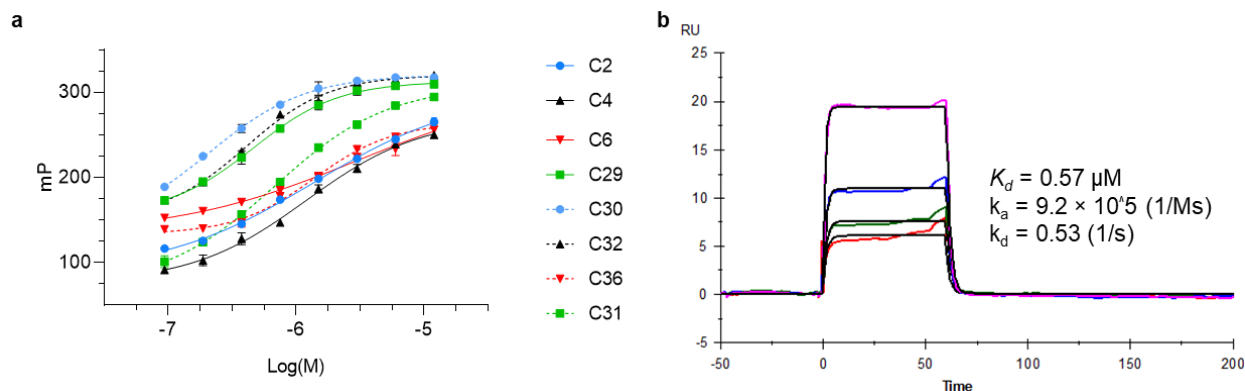
Extended Data Fig. 1 | Binding affinity of coumarin derivatives to SL5 RNA. a, Dose-response curves of coumarin derivatives in fluorescence polarization assay with in vitro transcribed SL5 RNA. All compounds were used at a concentration of 80 nM. Each data point represents the mean fluorescence polarization value of two independent replicates (N = 2). **b**, Surface plasmon resonance (SPR) binding analysis of **C30** with SL5 RNA. (Curve fitting is shown as black line. [SL5 RNA] = 0.075, 0.15, 0.3, and 0.6 µM).

630

631
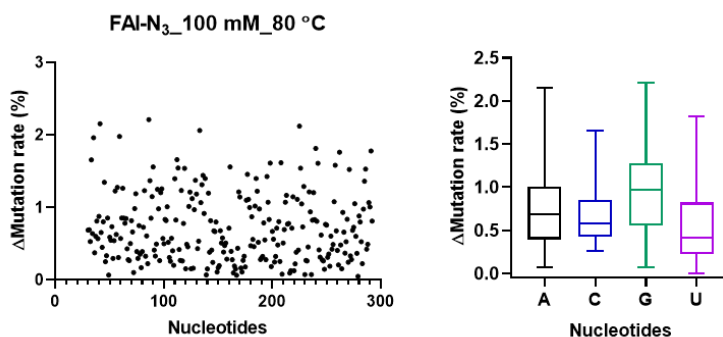
Extended Data Fig. 2 | Background Δmutation rate (FAI-N$_3$ – DMSO) of A, C, G, and U in denatured RNA treated with FAI-N$_3$. Denatured RNA was treated with **FAI-N$_3$** (100 mM) at 80 °C for 5 min in the denaturing buffer containing 90% formamide, 5 mM EDTA. Mutation rate was calculated with ShapeMapper2 software package[39]. RNA sequence is 5'-
aacuuccuuuauuuuccuuacaggguuuuAGACAAAAUCAAAAAGAAGGAAGGUGCUCACAUUCCUUAAAU
UAAGGAGUAAGUCUGCCAGCAUUAUGAAAGUGAAUCUUACUUUUGUAAAACUUUAUGGUUUGUGGAAAACAA
AUGUUUUUGAACAUUUAAAAAGUUCAGAUGUUAGAAAGUUGAAAGGUUAAUGUAAAACAAUCAAUAUUAAAGA
AUUUUGAUGCCAAAACUAUUAGAUAAAAGGUUAAUCUACAUCCCUACUAGAAUUCUCAUACUUAACUGGUUGG
UUGuguggaagaaacauacuuucacaauaaagagc. (lowercase = primer binding sequences).

641

642

643
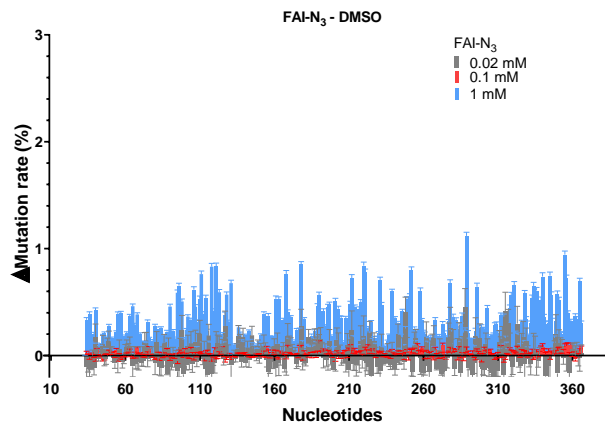
Extended Data Fig. 3 | Background Δmutation rate (FAI-N$_3$ – DMSO) of the SL5 sequence in total RNA extract treated with different concentrations of FAI-N$_3$. One data point (C75) was removed as an outlier as it had an abnormally high mutation rate (Z-score > 4.0) for the DMSO-treated sample.
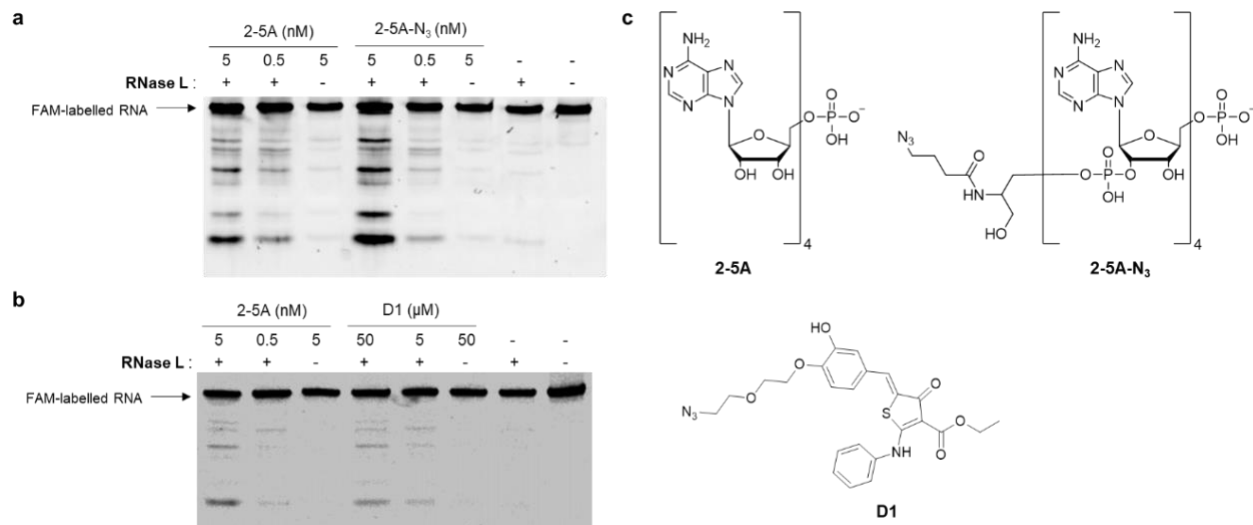
647

648
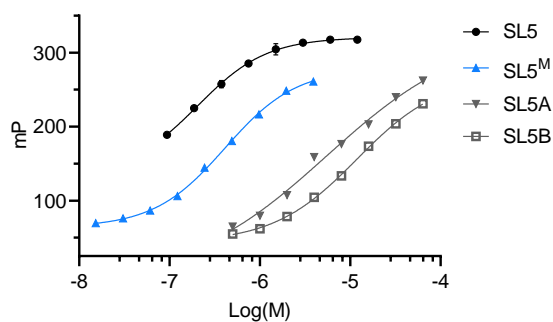
Extended Data Fig. 4 | Dose-response curves of **C30** (80 nM) in fluorescence polarization assay with SL5 RNA and its substructures. Each data point represents the mean fluorescence polarization value of two independent replicates (N = 2).

652

653

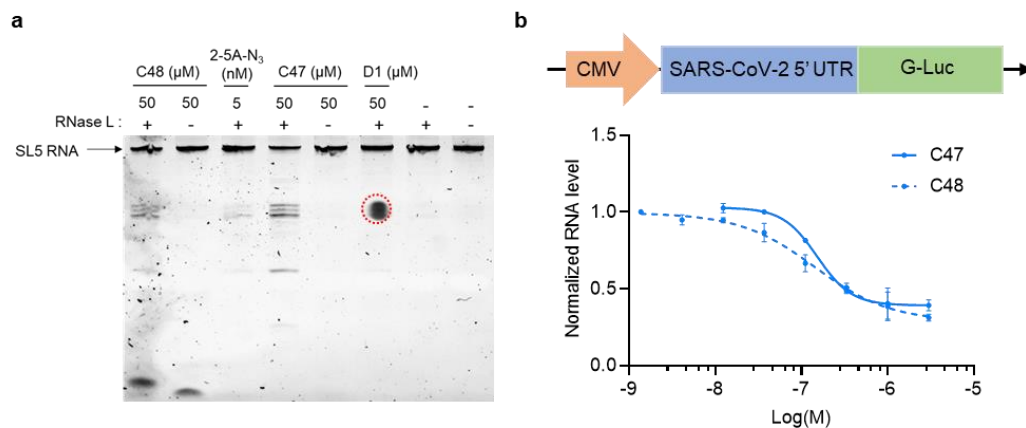**Extended Data Fig. 5 | In vitro RNase L degradation assay with a 5' 6-fluorescein-tagged model RNA containing multiple RNase L cleavage sites**. **a**, Comparison of RNA degradation activity of RNase L in the presence of **2-5A** and **2-5A-N₃** with no significant differential activity observed. **b**, Comparison of synthetic RNase L recruiter (D1) and 2-5A. The activity of **D1** in RNase L activation is ~ 10,000 times weaker than **2-5A**. **c**, Chemical structures of **2-5A**, **2-5A-N₃**, and **D1**.
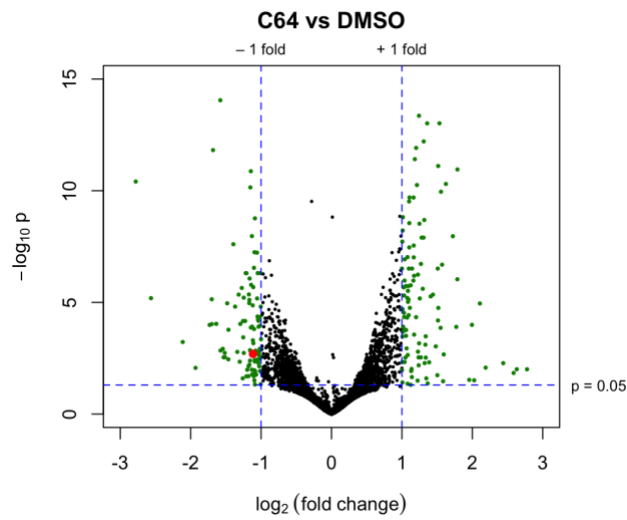

Extended Data Fig. 6 | RNA degrading activity of C47 and C48. **a**, Comparison of two RLR moieties in the RIBOTAC modality using the in vitro RNase L degradation assay with purified SL5 RNA (red circle is a staining artifact). **b**, Cellular activity of **C47** and **C48** in SARS-CoV-2 5' UTR expressing cells.

666

667 **Extended Data Fig. 7 |** Volcano plot of differential gene expression in SARS-CoV-2 5' UTR expressing cells treated
668 with C64 (3 µM). DMSO-treated cells were used as a control. Red spot = SARS-CoV-2 5' UTR transcript. The RNA-
669 seq analysis was performed with three biological replicates (N = 3).